JOURNAL OF Materials CHEMISTRY

Charge–discharge reaction mechanism of manganese vanadium oxide as a high capacity anode material for lithium secondary battery

Daishu Hara,[a] Junichi Shirakawa,[a] Hiromasa Ikuta,[a] Yoshiharu Uchimoto,[a] Masataka Wakihara,*[a] Takafumi Miyanaga[b] and Iwao Watanabe[c]

[a]*Department of Applied Chemistry, Graduate School of Science and Engineering, Tokyo Institute of Technology, 2-12-1, Okayama, Meguro-ku, Tokyo 152-8552, Japan. E-mail: mwakihar@o.cc.titech.ac.jp*
[b]*Department of Materials Science and Technology, Faculty of Science and Technology, Hirosaki University, Hirosaki, Aomori 036-8651, Japan*
[c]*Faculty of Science, Osaka Women's University, 2-1 Daisan-cho, Sakai, Osaka 590-0035, Japan*

Received 28th June 2002, Accepted 14th October 2002
First published as an Advance Article on the web 29th October 2002

Crystalline MnV_2O_6 with brannerite structure was synthesized by a classical solid-state reaction and its electrochemical reaction mechanism as an anode for a Li secondary battery was investigated. The reversible capacity of the MnV_2O_6 anode during the first cycle was about 670 A h kg^{-1}. An irreversible structural transformation into an amorphous phase *via* a rock-salt type structure was observed during the first Li insertion/removal reaction by X-ray diffraction (XRD) analysis. The charge compensation and the change in the local environmental structure during the Li insertion/removal were confirmed by X-ray absorption fine structure (XAFS) of Mn and V.

Introduction

It is urgent to investigate power sources with high specific energy density and long cycle life to meet current demand in the expanding market of portable electronic products. The lithium ion secondary battery has the capability to compete with the ever-growing energy necessity.[1,2] Commercially available lithium ion batteries generally employ layered transition metal oxides such as $LiCoO_2$[3] or $LiMn_2O_4$[4] as the cathode material and graphitized carbon as the anode material.[5] As the anode material, graphite provides a favorable low potential for the lithium insertion/removal and a long cycle life. However, its capacity is limited to about 370 A h kg^{-1} which is substantially smaller than that of metallic lithium,[6] and its rate property is not always enough for use as the anode of large-scale batteries in the near future.

In order to overcome these problems, numerous materials such as oxides,[7,8] nitrides[9,10] and intermetallics[11,12] have been studied as an anode material for lithium ion batteries, whose capacities are comparable or superior to those of carbonaceous materials. Among them, the oxide anodes are attractive, because of their high capacity and high rate performance. Vanadates especially have generated a new interest as an anode material.[13–15] In our previous papers,[14,15] we proposed electrochemical properties of MnV_2O_6 as a novel anode for a lithium ion secondary battery. The MnV_2O_6 compound had a monoclinic brannerite type structure with space group *C2/m*, and exhibited reversible capacity of about 800 A h kg^{-1}, which is more than twice that of graphite, and its rate property was three times that of graphite.[14] However, we observed an irreversible amorphization of MnV_2O_6 during the initial lithium insertion by XRD analysis, and this phenomenon makes it difficult to elucidate the reaction mechanism during the charge–discharge process.

In this study, the charge compensation of each transition metal and the change of local environmental structure during the Li insertion/removal of MnV_2O_6 were studied by careful measurements of XRD and XAFS of Mn and V.

Experimental

The sample, MnV_2O_6 was prepared by a conventional solid-state reaction at 600 °C for 3 days with starting materials of Mn_2O_3 and V_2O_5 (99.9% Soekawa chemicals). Mn_2O_3 was prepared by pyrolysis of $MnCO_3$ (99.9% Soekawa chemicals). The detail of the synthesis procedure was described in the previous paper.[15] The phase identification of the prepared sample was carried out by powder XRD using Rigaku RINT2500V with Cu K_α radiation at room temperature. Coulter SA3100 and LS200 measured the BET surface area and distribution of particle size of the compound, respectively.

The charge–discharge measurement of MnV_2O_6 was performed with a CR2032 coin-type cell. The working electrode was prepared using a mixture of 10 wt% polyvinylidenefluoride (PVDF) binder, 20 wt% acetylene black (conductive agent) and 70 wt% active material of MnV_2O_6. Further details of the procedure are described in the previous paper.[15] Lithium metal was used as the counter electrode. Electrochemical measurements were carried out galvanostatically at the rate of 70 μA mg^{-1} (of active material) at room temperature, and the relaxation time between charge and discharge was set at 20 min.

For all the electrochemical measurements, 1 M $LiClO_4$ dissolved in ethylene carbonate (EC)–diethyl carbonate (DEC) (volume ratio of 1 : 1) (as received from Tomiyama Pure Chemical Industries Ltd.) was used as the electrolyte. The cell assembling (Li|1 M $LiClO_4$ in EC–DEC|MnV_2O_6) and the sample preparation for *ex situ* XRD and *ex situ* XAFS measurements were operated in a glove box filled with argon gas.

The samples for the *ex situ* XRD and *ex situ* XAFS measurements were prepared by mixing 5 wt% polytetrafluoroethylene

DOI: 10.1039/b206255k

(PTFE) binder, 30 wt% acetylene black (conductive agent) and 65 wt% active material of MnV_2O_6. For *ex situ* XRD analysis, cells were fabricated by coupling the working electrode and the counter electrode of Li foil with microporous polypropylene film (Celgard2400) separator. The electrochemical measurements were carried out galvanostatically at the same rate of 70 μA mg^{-1} as the charge–discharge measurement with a CR2032 coin-type cell. The electrodes were removed at different depths of Li insertion/removal during the first cycle, and covered with polyethylene film to prevent reaction with moisture in the air. These samples were subjected to *ex situ* XRD measurements. The beaker-type cell was used for the preparation of samples for *ex situ* XAFS measurement. Li foil was used as the counter and reference electrodes with current collectors of Ni mesh (100 mesh, Niraco). Samples were prepared potentiostatically. The electrodes after Li insertion were removed from the cells and evacuated for drying. Samples were finely ground and mixed with boron nitride powder and pressed into pellets in order to obtain an optimum absorption jump ($\Delta\mu t \cong 1$) enough to be free from the thickness- and pinhole-effect. These pellets were sealed in polyethylene bags filled with argon gas and used for XAFS measurements.

XAFS measurements were performed at Photon Factory (PF, Tsukuba, Japan) with a ring energy of 2.5 GeV and a stored current of 440 mA in a transmission mode at room temperature. The data were collected at Mn and V *K*-edges on BL9A beam line[16,17] with a double crystal monochromator of Si(111). All data were analyzed using REX2000 software (Rigaku). For XANES spectra, the backgrounds were subtracted by extrapolation of the pre-edge absorptions for Mn and V, respectively using the Victoreen function ($DX^4 + CX^3$ + const).[18] The spectra were normalized at the values of edge jumps ($\Delta\mu t$) for each spectra of the absorption for Mn and V *K*-edges. The oxidation state of each ion was evaluated by comparing with the reference compounds of $MnCO_3$, Mn_2O_3 and Mn metal for manganese, and V_2O_5, V_2O_3 and V metal for vanadium. All compounds were purchased from Soekawa chemicals except for V_2O_3. V_2O_3 was synthesized by the decomposition of V_2O_5 under a H_2 atmosphere at 800 °C for 6 h. EXAFS data were analyzed as follows. The background absorption was calculated using the theoretical expression by the Victoreen function and the EXAFS vibration was estimated by interpolation of cubic spline function for Mn and V *K*-edges, respectively. The function was defined by varying the energy point of four nodes and the best removal was checked by further Fourier transform. The pseudoradial distribution functions (RDF) around the central atoms were obtained by Fourier transform of the weighted $\omega(k)k^3\chi(k)$ spectra, where $\omega(k)$ was window function (HANNING) defined between 3.5 and 13 $Å^{-1}$ for both Mn and V.

Results and discusson

The XRD pattern for the synthesized compound matched JCPDS data (card number 35-139).[19] All the Bragg peaks were indexed to proper miller indices by Rietan97 simulation, which confirmed that the synthesized sample forms a single phase of brannerite type structure MnV_2O_6 with monoclinic lattice.[15] The distribution of particle size is shown in Fig. 1. The maximum percentage particle size is 4.2 μm. The BET surface area is 0.542 m^2 g^{-1}. The brannerite structure consists of VO_6 pseudo-octahedra, which share opposite corners forming chains running parallel to the *b*-axis.[20] The VO_6 pseudo-octahedra in adjacent chains share the edges forming anion sheets parallel to (001) planes. Mn ions are situated between anionic sheets so that six oxygen atoms arranged in a distorted pseudo-octahedron coordinate each Mn ion. MnO_6 forms chain, which is parallel to the *b*-axis of the lattice. These chains are not linked with each other and provide rather open spaces

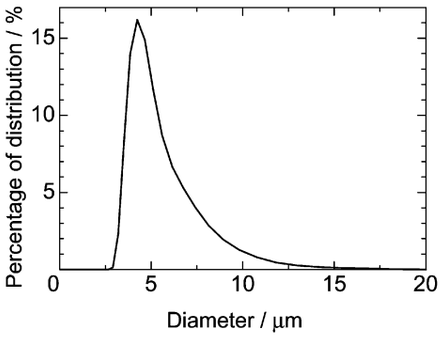

Fig. 1 The distribution of particle size of the MnV_2O_6 compound.

between the VO_6 sheets providing a favorable layered crystal structure for lithium insertion or extraction.

Mn and V *K*-edge XANES measurements for the synthesized powdered MnV_2O_6 were carried out to investigate the oxidation states of Mn and V. Fig. 2(a) shows the Mn *K*-edge XANES spectra of MnV_2O_6 together with those of $MnCO_3$ (Mn^{2+}) and Mn_2O_3 (Mn^{3+}) as references. The energy position of Mn *K*-edge jump of Mn_2O_3 is about 5 eV higher than that of $MnCO_3$. Therefore, the Mn K absorption edge shifts to a higher energy region with the increasing oxidation state of manganese.[21] Since the spectra of the edge jumps for $MnCO_3$ and MnV_2O_6 are very close to each other, Mn ions exist as close to Mn^{2+} in MnV_2O_6 compounds. V *K*-edge XANES spectra of V_2O_5 (V^{5+}), V_2O_3 (V^{3+}) and MnV_2O_6 presented in Fig. 2(b) illustrate that the valence of V in MnV_2O_6 is +5, because of quite similar behavior of MnV_2O_6 and V_2O_5. These oxidation state values for the transition metals in MnV_2O_6 are consistent with those in the previous reports.[14,15]

In order to obtain a charge–discharge profile of MnV_2O_6, the cell was subjected to several cycles in constant current mode at 70 μA mg^{-1}. Cutoff voltages were set at 0.01 V and 2.50 V. Fig. 3 shows the charge–discharge profiles of MnV_2O_6 at the first and second cycles. Solid circle symbols and the solid rhomboid symbols represent the voltages at which *ex situ* XRD and *ex situ* XAFS measurement of the electrodes were carried out, respectively. The insertion process of Li into the active material is defined as the charge process, while the reverse holds for the extraction process. The profiles in the figure indicate that the first Li insertion in MnV_2O_6 shows a large capacity of about 1000 A h kg^{-1}, which is quite large compared to that of graphite. The initial Li insertion profile of the MnV_2O_6 electrode has three plateau regions around 0.74 V, 0.56 V and 0.04 V during the first charge. Hereafter, the plateau at the

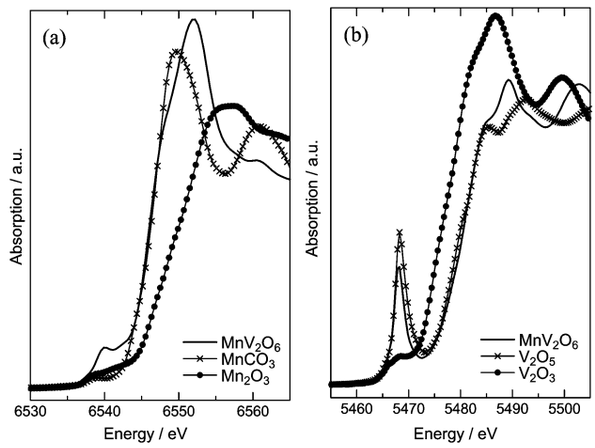

Fig. 2 XANES spectra of (a) Mn *K*-edge for MnV_2O_6, $MnCO_3$ and Mn_2O_3, (b) V *K*-edge for MnV_2O_6, V_2O_3 and V_2O_5.

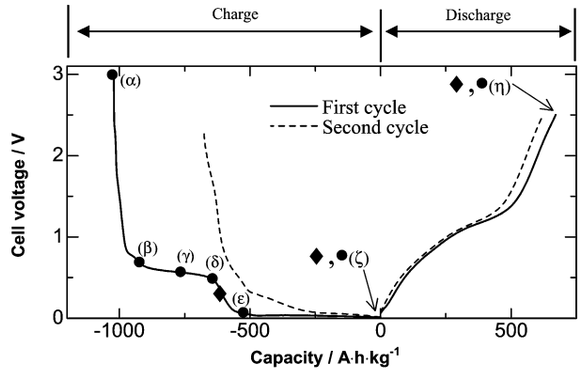

Fig. 3 The first and second charge–discharge curves of MnV_2O_6. Solid circles represents the cell voltage (α) before electrochemical measurement, (β) 0.65 V, (γ) 0.60 V, (δ) 0.50 V, (ε) 0.06 V, (ξ) 0.01 V and (η) 2.5 V that measured the XRD. The solid rhomboids represent the potential that is studied by the XAS electrode.

highest voltage, middle voltage and lowest voltage are defined as the first, the second and the third plateau, respectively. The first and second plateaus in the first lithium intercalation process of the electrode are not observed in the following cycles. This result is indicative of the different mechanism of insertion of Li ions into MnV_2O_6 between the first and the following cycles.

In order to investigate the structural change during the first cycle, the XRD patterns for the electrode before electrochemical measurement as well as those of various voltages during the first cycle are shown in Fig. 4(a). The peaks indicated by solid triangle symbols come from the polyethylene film that covers the surface of the electrode. The principal peaks still exist and no structural change is observed on the charged electrode at 0.65 V (β), which is the end of the first plateau. Therefore, the capacity of the corresponding plateau may be caused by the reduction of electrolyte to form solid electrolyte interface (SEI). The principal peaks decrease with insertion of lithium and all of them disappear completely at 0.01 V (ζ). When the electrode is discharged up to 2.50 V (η), no crystalline peaks are observed suggesting that the irreversible transformation from crystalline to amorphous phase occurs during the initial lithium insertion. This phenomenon of amorphization during the first lithiation was reported previously in several vanadates and molybdates.[22–25] Furthermore, a new Bragg peak appears around $2\theta = 42^\circ$ in the case of 0.60 V (γ) and it gradually disappears through subsequent insertion of lithium ion. In Fig. 4(b), the series of new Bragg peaks are shown at around $2\theta = 42^\circ$ and 62° with the simulated pattern of them by Rietan97. From the capacity of the second plateau (about 300 A h kg^{-1}), the amount of inserted Li^+ is estimated to be 3 mol per one molar MnV_2O_6 of the electrode ($Li_3MnV_2O_6$), since the insertion of one mol of Li^+ per one molar MnV_2O_6 corresponds to the capacity of 106 A h kg^{-1}. As the new Bragg peaks are similar with those of typically observed ones for the rock salt type structure,[26] the simulation of $Li_3MnV_2O_6$ having the rock-salt type structure is performed as follows: the ionic radii of Shannon[27] are used for Li(1+), Mn(2+), V(3+) and O(2−) whose oxidation states are described in the latter half of this paper, assuming that (1) the structure is rock-salt type (S.G. *Fm3m*), and that (2) all cations (Li, Mn and V ions) and the anion (O) distribute on the cation site and anion site, respectively, of the rock-salt type structure. The obtained theoretical lattice constant of $Li_3MnV_2O_6$ is 4.32 Å calculated from the sum of the average for each radius of cation and anion, and the simulated pattern by Rietan97 is shown in Fig. 4(b). The broad peak positions of the samples ((δ) 0.50 V or (ε) 0.06 V) are $2\theta = 42^\circ$ and 61°. However another peak around $2\theta = 36^\circ$ is estimated to exist,

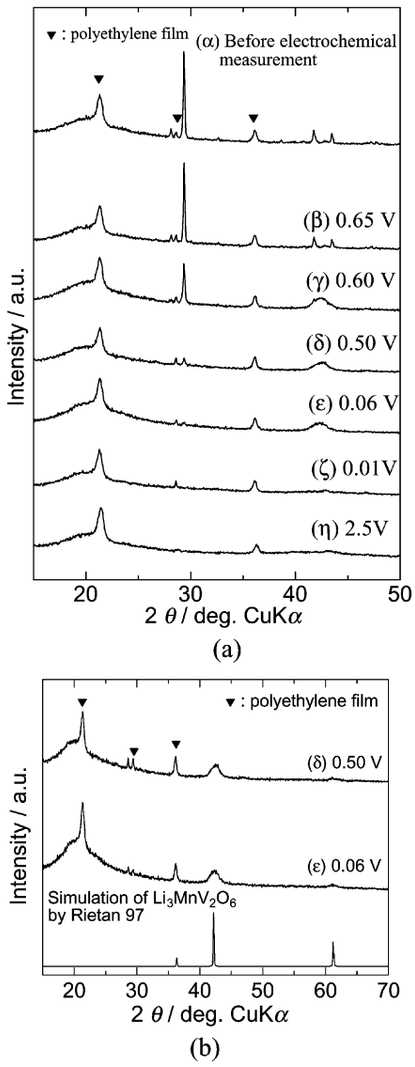

Fig. 4 XRD patterns of the electrodes at (a) various cell voltages during the first cycle, (b) 0.50 and 0.06 V together with the simulated diffraction pattern by Rietan97.

it is thought to be veiled by the peak of polyethylene film in Fig. 4(b). The simulation by Rietan97 indicates that the assuming structure is consistent with the experimental one. Furthermore, the cubic lattice constant of the active material is calculated as 4.3 Å from the new Bragg peak of $2\theta = 42^\circ$ observed at 0.50 V, which corresponds to (200) plane. This value is quite close to the theoretical one (4.32 Å). Therefore, it is assumed that the brannerite MnV_2O_6 transforms to amorphous *via* a highly symmetrical structure such as a rock-salt type structure during the first lithium insertion.

To evaluate the origin of irreversible capacity, the first charge–discharge curves at several cutoff voltages are presented in Fig. 5. Discharge capacities obtained from the cutoff voltages at 0.70 V and 0.50 V are almost zero. This means that inserted Li ion by 0.50 V cannot be extracted. On the other hand, a large discharge capacity is observed in the case of 0.01 V cutoff voltages. A large reversible capacity arises from the third plateau, and this plateau has almost the same Li extraction capacity up to 2.5 V.

The Mn *K*-edge XANES of the electrode during the first Li insertion/removal and second insertion processes are shown in Fig. 6(a) together with Mn metal as the reference. In the figure, we can observe that the valence of Mn is still +2 in the spectrum at 0.4 V, which corresponds to the end of the second

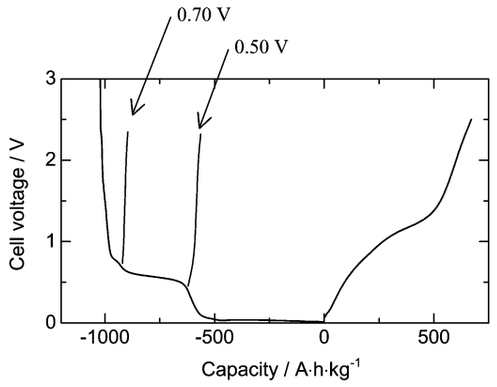

Fig. 5 The charge–discharge curves of MnV_2O_6 at various cutoff voltages.

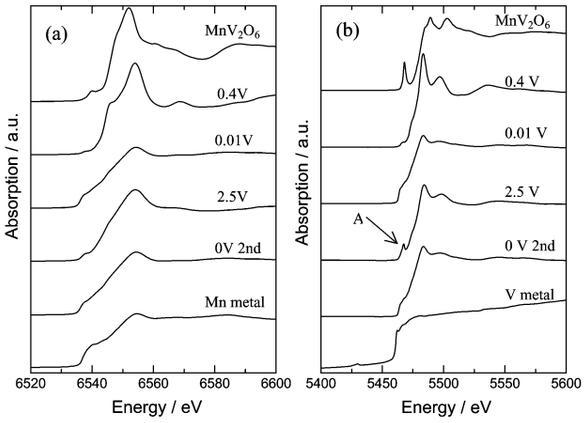

Fig. 6 XANES spectra of the electrodes at various voltages for (a) Mn *K*-edge, (b) V *K*-edge.

plateau, because the oxidation state of Mn (+1) is difficult to imagine even though the position of the edge jump shifts slightly to a lower energy region compared with that of before the electrochemical measurement. Furthermore, the shape of the peak changes at this voltage. This phenomenon also confirms the transformation from brannerite to new phase on the second plateau, which is observed by *ex situ* XRD measurement in Fig. 4(b). The valence of Mn of the fully lithiated MnV_2O_6 electrode at 0.01 V is estimated to be zero by comparison with metallic Mn as the reference (Fig. 6(a)). A slight shift of the position of the *K*-edge towards a higher energy region is observed when the electrode is discharged to 2.5 V. However, the manganese oxidation state is still considered to be almost zero. Then, Mn retains zero when it is re-charged up to 0.01 V. The V *K*-edge XANES during the Li insertion/removal is shown in Fig. 6(b). When the electrode is lithiated up to 0.4 V, the valence of V changes to +3 because the energy of edge jump is similar to V_2O_3 in Fig. 7. Furthermore in Fig. 6(b), the progressive decrease of the pre-peak intensity is observed at 0.4 V which confirms the change of the symmetry of vanadium coordination from distorted pyramidal to more symmetrical octahedron, and it supports the transformation from brannerite to new phase as is observed by *ex situ* XRD measurement in Fig. 4(b). The edge position suggests that the valence of V is reduced to +2 at the fully charged voltage of 0.01 V, since the edge jump of the spectra exists in higher energy region than V metal. However, it is reduced more than at 0.4 V as mentioned above. At the end of the initial discharge up to 2.5 V, the oxidation state of vanadium is +4, because of (1) the edge shift toward higher energy region compared with that of 0.01 V and (2) the

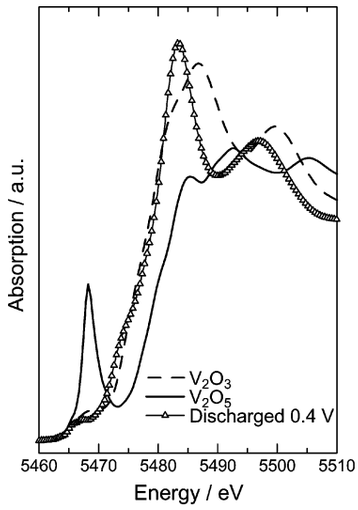

Fig. 7 V *K*-edge XANES spectra for the electrodes at 0.4 V and 2.5 V during the first charge and discharge, respectively with V_2O_3 and V_2O_5 as references.

appearance of pre-edge peak,[28] which is arrowed as "A" in Fig. 6(b). Then, V is reduced to +2 again during the following lithiation at 0.01 V on the second cycle. It is revealed that V is reversibly redoxed from +2 to +4 during the cycle whereas manganese valence exhibits no change after the initial lithium insertion to zero volt.

Even if we assume that the valence change of V is between +2 and +4, it is not sufficient to explain total capacity of MnV_2O_6 on the first discharge (670 A h kg^{-1}). Apart from lithium insertion to brannerite MnV_2O_6 with a large amount of lithium, the mechanism of lithium insertion is reported in other oxide anode system of RVO_4 (R = In, Ce, Fe, Al, Y).[29] In the literature, it is suggested that oxygen acts as a redox center of Li–O bonds thereby leading to an enhancement in observed capacity. We could assume a similar mechanism during the charge–discharge to understand the large capacity exhibited by MnV_2O_6. Accordingly, it can be stated that the 2*p* orbital of oxygen may play an important role for the compensation of charge equivalence besides transition metals during the insertion and extraction of Li.

From both Mn and V *K*-edge XAFS, EXAFS analyses can be performed. Mn *K*-edge EXAFS spectra of $k^3\chi(k)$ for the electrodes at various potential are shown in Fig. 8(a). The extent of the spectra is limited from 3.5 $Å^{-1}$ to 13.0 $Å^{-1}$, since the window function $\omega(k)$ is adjusted in this range. In the case of the electrode before electrochemical measurement and that

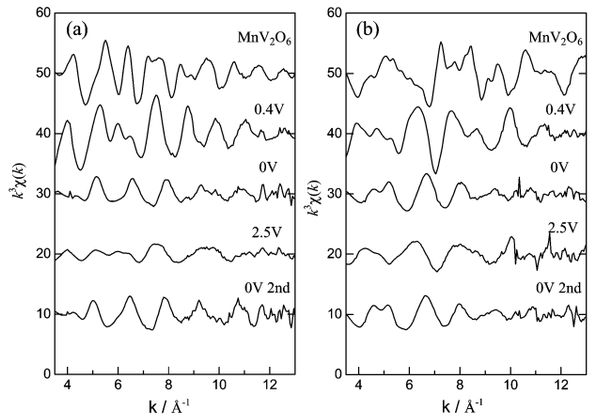

Fig. 8 EXAFS $k^3\chi(k)$ spectra of the electrodes at various voltages for (a) Mn *K*-edge and (b) V *K*-edge.

after charging up to 0.4 V, the spectra have distinctive vibrations indicating that these oxides have ordered crystal structures. On the other hand, the amplitude of the spectra are weak for the electrodes at 0.01 V and 2.5 V during the first cycle and then 0.01 V during the second cycle, because of their low crystallinity even in the extent of second or third nearest atoms. Fig. 8(b) shows V *K*-edge EXAFS spectra of $k^3\chi(k)$ for the electrodes at various potential. The window function $\omega(k)$ is defined from 3.5 Å to 13.0 Å as well as the manganese spectra. The tendency of behavior for the spectra of the electrodes is similar to that of Mn as mentioned in Fig. 8(a).

Fig. 9 represent the Fourier transforms of the Mn *K*-edge EXAFS spectra for the electrode at various potentials during (a) the first lithium insertion, (b) the following extraction and re-insertion, respectively. Since these Fourier transforms are not corrected for the phase shifts,[30] the peak positions in the figures, which will be mentioned later, are not equivalent to the actual bond length of the atoms. In the case of the electrode before electrochemical measurement, the first peak located around 1.7 Å corresponds undoubtedly to Mn–O distances and the second one centered on 3.0 Å can be attributed to Mn–Mn and/or Mn–V distance in Fig. 9(a).[24] The Mn–Mn and/or Mn–V distances of the MnV_2O_6 electrode is shortened at 0.4 V compared with that before electrochemical measurement. When the electrode is charged up to 0.01 V, the spectrum is constituted of a single peak centered at 2.1 Å. This indicates that the local environmental structure of the second nearest atoms around Mn no longer exist in the amorphous phase of active material at this potential. The observed peak is considered to be Mn–Mn and/or Mn–V distance, because the manganese oxidation state is zero at this potential as mentioned previously. In Fig. 9(b), the peak splits into two peaks centered around 1.6 and 2.7 Å which correspond to Mn–O distances and Mn–Mn and/or Mn–V distance respectively in the electrode after following discharge up to 2.5 V. Although the average valence of Mn is still almost zero, a slight oxidation of Mn, which is observed from XANES spectra in Fig. 6(a), affects the appearance of the Mn–O peak at 2.5 V. Then, the peaks unite into a single peak again when the electrode is re-charged up to 0.01 V during the second cycle and the structure has a similar shape to that of 0.01 V during the first cycle.

Fig. 10 represents the Fourier transforms of the V *K*-edge

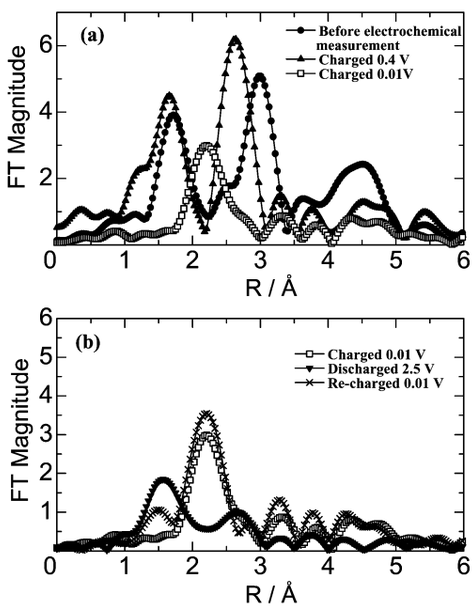

Fig. 9 The Fourier transforms of the Mn *K*-edge EXAFS spectra for the electrodes at various voltages. (a) The first charge. (b) Following discharge and re-charge.

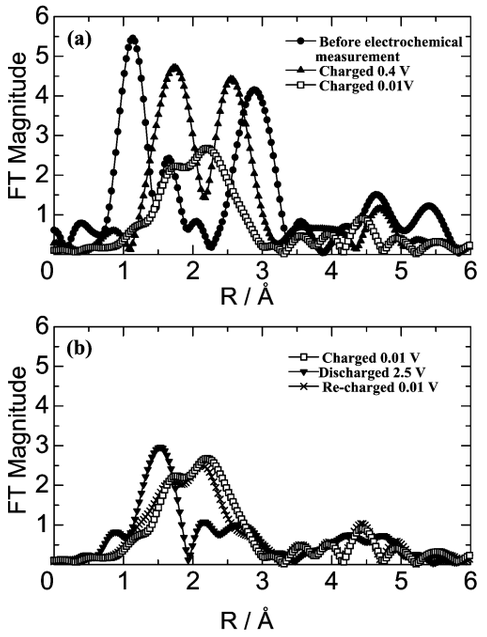

Fig. 10 The Fourier transforms of the V *K*-edge EXAFS spectra for the electrodes at various voltages. (a) The first charge, (b) Following discharge and re-charge.

EXAFS spectra for MnV_2O_6 at various potentials. The Fourier transforms are not corrected for the phase shifts. In the case of the electrode before electrochemical measurement in Fig. 10(a), the first peak located at the atomic distance of 1.2 and 1.6 Å comes undoubtedly from V–O distances.[24] The second one centered at 2.9 Å can be attributed to the V–Mn and/or V–V distances. The peak shifts of V–Mn and/or V–V distances exhibit the same tendency with Mn with insertion and removal of Li in the active material at 0.4 V. At the same time, the distance of V–O becomes longer than that of the electrode before electrochemical measurement. Then, the peaks wrap over together at 0.01 V. These united peaks correspond to the mixture of V–O distances and V–Mn and/or V–V distances, since V has the valence of +2 from the XANES spectra at this potential in Fig. 6(b). Then, these peaks are separated clearly at the end of charge at 2.5 V in Fig. 10(b), and this result persuades the oxidation of vanadium. When the electrode is re-charged to 0.01 V, the structure of peaks are almost the same as that of firstly charged ones.

These results of the Fourier transforms for Mn and V indicate that the local environmental structure around the transition metals reversibly changes during the cycles, even though the long-range structure cannot be observed by XRD after the initial lithiation. Furthermore, the local environments of 2.5 V during the discharge for both Mn and V in the active material differ from those in MnV_2O_6 electrode before electrochemical measurement. This phenomenon accounts for the irreversible capacity in the first cycle, which is observed in Fig. 5, because of the different lattice potentials between the electrode before electrochemical measurement and that at 2.5 V during discharge.

Fig. 11 represents the comparison of the Fourier transforms of Mn and V *K*-edge EXAFS spectra of the electrodes at 0.4 V during the first lithiation. The Fourier transforms are not corrected for the phase shifts. The positions of the first (metal–O) and second (metal–metal) both two individual peaks are almost consistent between Mn and V, respectively. This phenomenon also supports the appearance of the rock-salt type structure at the voltage that is observed by *ex situ* XRD measurement.

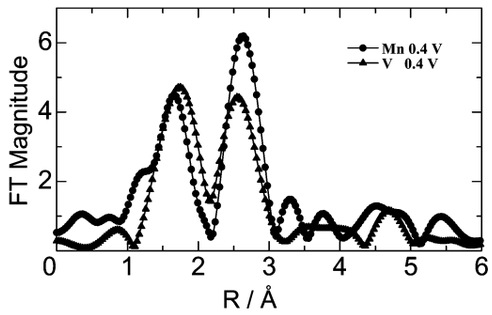

Fig. 11 The Fourier transforms of the Mn and V *K*-edge EXAFS spectra for the electrodes at 0.4 V during the first charge.

Conclusions

MnV_2O_6 was synthesized by a classical solid state reaction. XRD analysis indicated that MnV_2O_6 had a brannerite type structure and it irreversibly transformed to amorphous phase *via* rock-salt type structure during the initial lithium insertion. *K*-edge XANES spectra of MnV_2O_6 electrodes at various voltages suggested that the oxidation state of V changes from +5 to +2 during the initial lithium insertion and from +2 to +4 during the lithium extraction, whereas that of Mn changes from +2 to zero during the initial lithium insertion and then remains unchanged during the following cycles. EXAFS spectra of Mn and V revealed that the local environmental structure reversibly changes during the Li insertion/removal with MnV_2O_6.

Acknowledgements

The authors thank Photon Factory for providing the beam time (project 2001G120). This work was supported by Grant-in-Aid for Scientific Research on Priority Areas (B) (No. 740) "Fundamental Studies for Fabrication of All Solid State Ionic Devices" from Ministry of Education, Culture, Sports, Science and Technology.

References

1 M. Wakihara, *Mater. Sci. Eng.*, 2001, **R33**, 109.
2 Y. Nishi, *J. Power Sources*, 2001, **100**, 101.
3 T. Nohma, H. Kurokawa, M. Uehara, M. Takahashi, K. Nishio and T. Saito, *J. Power Sources*, 1995, **54**, 522.
4 M. Hosoya, H. Ikuta and M. Wakihara, *Solid State Ionics*, 1998, **111**, 153.
5 K. Sato, M. Noguchi, A. Demachi, N. Oki and N. Endo, *Science*, 1994, **264**, 22.
6 V. R. Koch, J. L. Goldman, C. J. Mattos and M. Mulvaney, *J. Electrochem. Soc.*, 1982, **129**, 1.
7 M. Baba, N. Kumagai, N. Fujita, K. Ohta, K. Nishidate, S. Komaba, H. Groult, D. Devilliers and B. Kaplan, *J. Power Sources*, 2001, **97–98**, 798.
8 P. P. Prosini, M. Carewska, S. Loreti, C. Minarini and S. Passerini, *Int. J. Inorg. Mater.*, 2000, **2**, 365.
9 Y. Takeda, M. Nishijima, M. Yamahata, K. Takeda, N. Imanishi and O. Yamamoto, *Solid State Ionics*, 2000, **130**, 61.
10 S. Suzuki, T. Shodai and J. Yamaki, *J. Phys. Chem. Solids*, 1998, **59**, 331.
11 A. Anani, S. C. Baker and R. A. Huggins, *J. Electrochem. Soc.*, 1987, **134**, 3098.
12 M. Mohamede, S.-J. Lee, D. Takahashi, M. Nishizawa, T. Itoh and I. Uchida, *J. Electrochem. Acta*, 2001, **46**, 1161.
13 E. Baudrin, S. Laruelle, S. Denis, M. Touboul and J.-M. Tarascon, *Solid State Ionics*, 1999, **123**, 139.
14 S.-S. Kim, H. Ikuta and M. Wakihara, *Solid State Ionics*, 2001, **139**, 57.
15 D. Hara, H. Ikuta, Y. Uchimoto and M. Wakihara, *J. Mater. Chem.*, 2002, **12**, 2507.
16 M. Nomura and A. Koyama, *J. Synchrotron Radiat.*, 1999, **6**, 182.
17 M. Nomura and A. Koyama, *Nucl. Instrum. Methods Phys. Res. Sect. A*, 2001, **467–468**, 733.
18 J. A. Victoreen, *J. Appl. Phys.*, 1948, **19**, 855.
19 R. Kozlowski, J. Ziolkowski, K. Mocala and J. Haber, *J. Solid State Chem.*, 1980, **35**, 1.
20 K. Mocala and J. Ziolkowski, *J. Solid State Chem.*, 1987, **69**, 299.
21 J. R. Bargar, B. M. Tebo and J. E. Villinski, *Geochim. Cosmochim. Acta*, 2000, **64**, 2775.
22 D. Guyomard, C. Sigala, A. G. L. Salle and Y. Piffard, *J. Power Sources*, 1997, **68**, 692.
23 C. Rossignol, G. Ouvrad and E. Baudrin, *J. Electrochem. Soc.*, 2001, **148**(8), A869.
24 S. Laruelle, P. Poizot, E. Baudrin, V. Briois, M. Touboul and J-M. Tarascon, *J. Power Sources*, 2001, **97–98**, 251.
25 S.-S. Kim, S. Ogura, H. Ikuta, Y. Uchimoto and M. Wakihara, *Solid State Ionics*, 2002, **146**, 249.
26 R. E. Loehman, C. N. R. Rao and J. M. Horig, *J. Phys. Chem.*, 1969, **73**, 1781.
27 R. D. Shannon, *Acta Crystallogr.*, 1976, **A32**, 751.
28 J. Wong, F. W. Lytle, R. P. Messmer and D. H. Maylotte, *Phys. Rev. B.*, 1984, **30**, 5596.
29 S. Denis, E. Baudrin, M. Touboul and J.-M. Tarascon, *J. Electrochem. Soc.*, 1997, **144**, 4099.
30 D. C. Creagh, *International Tables for Crystallography*, ch. 4, Section 4.2.3., The International Union of Crystallography, Kluwer Academic Publishers, Dordrecht/Boston/London, 1995, **vol. C**.